Editors' Suggestion

Observation of body-centered cubic iron above 200 gigapascals

Zuzana Konôpková,[1,*,†] Eric Edmund,[2,*,‡] Orianna B. Ball,[3] Agnès Dewaele,[4,5] Hélène Ginestet,[6] Rachel J. Husband,[1,7] Nicolas Jaisle,[8] Cornelius Strohm,[7] Madden S. Anae,[9] Daniele Antonangeli,[10] Karen Appel,[1] Marzena Baron,[11] Silvia Boccato,[10] Khachiwan Buakor,[1] Julien Chantel,[6] Hyunchae Cynn,[12] Anand P. Dwivedi,[1] Lars Ehm,[9] Konstantin Glazyrin,[7] Heinz Graafsma,[7] Egor Koemets,[13,14] Torsten Laurus,[7] Hauke Marquardt,[13] Bernhard Massani,[3] James D. McHardy,[3] Malcolm I. McMahon,[3] Vitali Prakapenka,[15] Jolanta Sztuk-Dambietz,[1] Minxue Tang,[7] Tianqi Xie,[16,9] Zena Younes,[3] Ulf Zastrau,[1] Alexander F. Goncharov,[2] Clemens Prescher,[17] Ryan S. McWilliams,[3] Guillaume Morard,[10,8] and Sébastien Merkel[6]

[1]*European XFEL, Schenefeld, Germany*
[2]*Earth & Planets Laboratory, Carnegie Science, 5251 Broad Branch Rd NW, Washington, DC 20015, USA*
[3]*SUPA, School of Physics and Astronomy, and Centre for Science at Extreme Conditions (CSEC), The University of Edinburgh, Peter Guthrie Tait Road, Edinburgh EH9 3FD, United Kingdom*
[4]*CEA, DAM, DIF, 91297 Arpajon, France*
[5]*Université Paris-Saclay, CEA, Laboratoire Matière en Conditions Extrêmes, 91680 Bruyères-le-Châtel, France*
[6]*Univ. Lille, CNRS, INRAE, Centrale Lille, UMR 8207 - UMET - Unité Matériaux et Transformations, F-59000 Lille, France*
[7]*Deutsches Elektronen-Synchrotron DESY, Notkestr. 85, 22607 Hamburg, Germany*
[8]*ISTerre, Université Grenoble Alpes, CNRS, Grenoble, France*
[9]*Department of Geosciences, Stony Brook University, Stony Brook, New York 11794-2100, USA*
[10]*Sorbonne Université, Muséum National d'Histoire Naturelle, UMR CNRS 7590, Institut de Minéralogie, de Physique des Matériaux et de Cosmochimie (IMPMC), Paris, France*
[11]*Sorbonne Université, CNRS, Laboratoire Chimie de la Matière Condensée de Paris (LCMCP), 4 place Jussieu, 75005 Paris, France*
[12]*Lawrence Livermore National Laboratory, Physical and Life Science Directorate, Livermore, California 94550, USA*
[13]*Department of Earth Sciences, University of Oxford, 3 South Parks Road, OX1 3AN Oxford, United Kingdom*
[14]*Diamond Light Source, Didcot, United Kingdom*
[15]*Center for Advanced Radiation Sources, The University of Chicago, Chicago, Illinois 60637, USA*
[16]*Department of Geological Sciences, University of Saskatchewan, Saskatoon, Canada*
[17]*University of Freiburg, Freiburg, Germany*

(Received 21 February 2025; revised 13 July 2026; accepted 15 July 2026; published 10 August 2026)

The crystallographic structure of iron under extreme conditions is a key benchmark for state-of-the-art experimental and computational methods. Moreover, it plays a crucial role in our understanding of planetary cores, as it strongly influences the interpretation of observational data and, consequently, our knowledge of their internal structure and dynamics. However, even the crystal structure of pure solid iron under Earth's core conditions remains uncertain, with the commonly expected hexagonal close-packed phase being energetically competitive with several cubic structures. In this study, iron was compressed in a diamond anvil cell to pressures exceeding 200 GPa and dynamically probed near its melting point using MHz-frequency x-ray pulses from the European X-ray Free-Electron Laser. In the pressure range between 120 and 160 GPa, the high temporal resolution of the structural snapshots at elevated temperatures revealed the face-centered cubic phase, extending its observed stability to higher pressures than previously reported. Brief appearances of intermediate or disordered phases, including body-centered cubic (bcc) and stacking-faulted structures, were also observed. Above 230 GPa, new diffraction reflections emerged at high temperatures and are interpreted as evidence for the nucleation of a previously unreported phase, which subsequently evolved into a powderlike diffraction pattern characteristic of the bcc structure. The unprecedented time resolution of the structural data acquired during rapid heating and cooling cycles provides insights into the kinetics and mechanisms of phase transformations in iron at these extreme pressures.

DOI: 10.1103/kxnf-6c5y

I. INTRODUCTION

Observations of elastic anisotropy in Earth's inner core have motivated numerous investigations into the phase diagram of iron at these conditions—330 to 360 GPa and

*These authors contributed equally to this work.
†Contact author: zuzana.konopkova@xfel.eu
‡Present address: Universität Münster, Münster, Germany.

exceeding 5000 K—using a variety of experimental [1–10] and *ab initio* techniques [11–19]. At the heart of this question is whether or not crystalline phases other than hexagonal close-packed (hcp) iron are stable at inner core conditions.

Theoretical studies indicate that the Gibbs free energies of the various high-pressure polymorphs of iron are very similar at core conditions. The hcp structure is unambiguously the stable phase of iron at moderate temperatures above 13 GPa [11]; however, face-centered cubic (fcc) and body-centered cubic (bcc) structures have been proposed to become energetically competitive with the hcp structure at temperatures close to the melting point of iron at inner core pressures [12–19]. The need for large simulation sizes presents a challenge, as the mechanical stability of bcc iron is highly dependent on these conditions. Self-diffusion, characterized by collective atomic motion, has been reported for both bcc iron [13,19,20] and hcp iron [3] just below the melting point at high pressures. Recent *ab initio* simulations augmented with machine learning have demonstrated the mechanical stability of the bcc structure of pure iron under Earth's core conditions. However, its thermodynamic stability compared to an hcp structure appears to be enhanced only in the presence of impurities [19].

Additional experimental investigations into the structure of solid iron at Earth's core conditions are required, particularly at temperatures close to melting, but measuring the structure of iron at such conditions is experimentally challenging. Dynamic compression of iron provides one method to investigate iron's phase stability above 200 GPa. Crystal structure measurements have been performed in single shock experiments [4–6,21] and in more complex compression experiments [8]. While these studies observe only an hcp structure up to melting, reaction kinetics and the shifting of phase stabilities due to high strain rates and short experimental timescales can potentially lead to discrepancies between phase transitions encountered during dynamic compression and static compression experiments [22,23].

Static compression experiments offer an alternative avenue to investigate the structure of iron at core conditions [9,10,24–26]. However, despite being able to access longer timescales and hence better approach thermodynamic equilibrium conditions, static compression experiments suffer from challenges due to the large temperature gradients present in the samples and the difficulties of avoiding chemical contamination of the compressed iron sample [9,27,28].

These challenges necessitate the use of new experimental tools and capabilities with which to probe phase transitions at extreme conditions. Experimental timescales need to be sufficiently short to suppress unwanted chemical reactions, while being sufficiently long to minimize the effects of transition kinetics (i.e., microseconds); highly monochromatic x rays which probe the sample with high time resolution are needed to better resolve structural transition details, including difficult to detect structural intermediary states. Such experiments have been carried out at the High Energy Density (HED) beamline of the European X-ray Free Electron Laser (EuXFEL) using the diamond anvil cell (DAC) platform [29–31] as part of the #3063 community proposal.

II. METHODOLOGY

The DACs were prepared at initial pressures ranging from 10 to 218 GPa using rhenium gaskets and either KCl or SiO_2 as the pressure-transmitting medium. Samples were fabricated from 5-μm-thick iron foils (Sigma-Aldrich, purity 99.85%, part #GF19019000), which were cut into disks of 10, 20, or 40 μm diameter using a femtosecond laser at CEA, Bruyères-le-Châtel, France, and subsequently distributed among the participating institutions.

Of these, five samples were investigated at pressures above 120 GPa: CDMVA9 and CDMX10, both prepared at CEA, Bruyères-le-Châtel, France, with initial pressures of 134 and 122 GPa, respectively; BetsaA, prepared at the University of Lille, France, with an initial pressure of 152 GPa; HIBEF38, prepared at EuXFEL in Hamburg, Germany, with an initial pressure of 208 GPa; and CC273, prepared at the Earth & Planets Laboratory, Carnegie Institution for Science, Washington, DC, USA, with an initial pressure of 218 GPa.

HIBEF38 employed two identical beveled diamond anvils with 40 μm culets, whereas CC273 utilized toroidal diamond anvils fabricated using a focused ion beam. The KCl pressure medium was stored in a vacuum oven prior to sample loading.

All cells were characterized by x-ray diffraction and their initial pressures were determined at the P02.2 beamline of PETRA III, Hamburg, Germany. Measurements were performed using monochromatic x rays with a wavelength of 0.2909 Å and a PerkinElmer XRD 1621 flat-panel detector comprising 2048×2048 pixels of 0.2×0.2 mm^2. The detector was positioned 416 mm from the sample.

Pressures were estimated using the equation of state of iron reported by Dewaele *et al.* [32]. Experimental details and metrology for the lower-pressure measurements are summarized in Ref. [33].

At EuXFEL, during the #3063 community proposal on beamline HED, 18 keV x-ray pulse trains were delivered to the sample chamber and focused to a spot size of 4–7 μm FWHM. Each pulse train comprised 352 individual pulses separated by 222 ns [Fig. 1(a)], with each x-ray pulse having a duration of less than 30 fs [30]. The 4.5 MHz repetition rate of the x-ray pulses resulted in progressive heating of the sample, as the rate of energy deposition by x-ray absorption exceeded the rate of heat diffusion from the sample over the 78 μs duration of the pulse train.

The structural evolution of the sample was monitored by recording x-ray diffraction patterns using the Adaptive Gain Integrating Pixel Detector (AGIPD) [34]. The femtosecond pulse duration of the EuXFEL x-ray pulses enabled atomic-scale snapshots of the material within the DAC, with exposure times significantly shorter than the characteristic timescale of lattice vibrations (approximately 1 ps). Because scattering occurs before any appreciable heating induced by the same pulse, each diffraction pattern records the sample structure immediately prior to the energy deposition of that pulse. Consequently, each snapshot represents the structure of the sample as it cools following excitation by the preceding pulse.

This experimental setup was complemented by streaked optical pyrometry (SOP), which monitored the time-resolved thermal emission from the sample throughout the experiment [31]. The SOP detection system consists of a visible-light

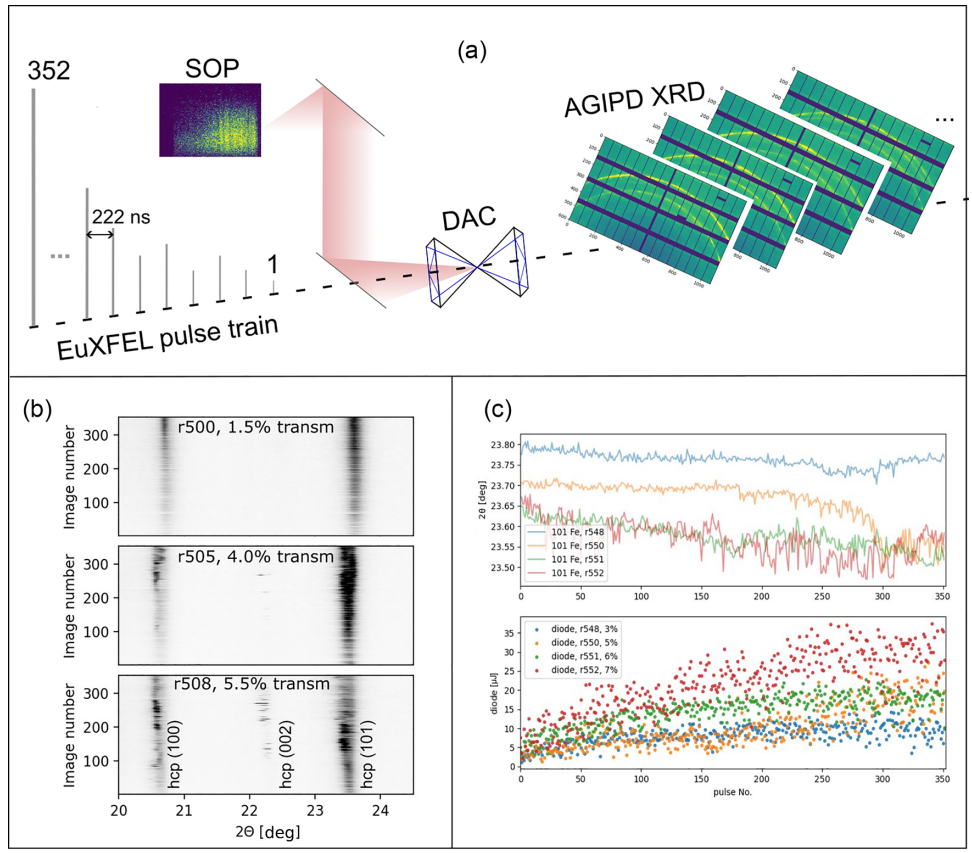

FIG. 1. (a) Experimental setup. A train of 352 x-ray pulses probes and heats the sample at intervals of 222 ns. (b) Stacked integrated diffraction patterns from the CC273 DAC (initial pressure: 218 GPa), acquired with progressively increasing x-ray transmission (i.e., increasing pulse energy) from the top panel to the bottom panel. Recrystallization begins above 4% transmission, as indicated by the more frequent appearance of the hcp-Fe 002 reflection. (c) HIBEF38 DAC (starting pressure 208 GPa): the 2θ position of 101 hcp-Fe peak during successive trains with increasing x-ray energies (shown in the bottom panel) shows sample annealing indicated by lower 2θ value of the first diffraction of the train, stabilizing at 23.65° (green and red data).

spectrometer coupled to a streak camera. The interaction region on the sample is imaged onto the entrance slit of the spectrometer, where the emitted light is dispersed by a diffraction grating over the 500–800 nm wavelength range and projected onto the streak camera photocathode. A streak image is produced by sweeping the signal in time, enabling measurement of temporal variations in the emitted light intensity over the duration of the x-ray pulse train. A 100 μs sweep window was used to capture the entire pulse train.

Structural information on high-pressure Fe at elevated temperatures is accessible only during cooling following heating induced by the preceding x-ray pulse. Consequently, the temperatures immediately after x-ray energy deposition may be significantly higher than those measured at the time of probing. To visualize the transient temperature evolution within the sample during the pulse train, we performed finite element analysis (FEA) using COMSOL Multiphysics, following an approach similar to that of Meza-Galvez *et al.* [35].

The model simulated heat conduction in a two-dimensional axisymmetric cylindrical geometry comprising a 2-μm-thick Fe sample thermally isolated from the diamond anvils by 1-μm-thick KCl layers. The x-ray beam profile was approximated by a Gaussian distribution with a standard deviation (σ) of 3 μm. The energies of all 352 x-ray pulses were derived from measurements of scattered radiation from a thin diamond window using fast photodiodes positioned upstream of the interaction point. These measurements were calibrated to absolute pulse energies using x-ray gas monitors (XGM) [36] prior to the experiment.

The material properties used in the simulations are summarized in Table I.

III. RESULTS

Initially, the experiment was tested on multiple diamond anvil cells with Fe samples loaded in either KCl or SiO2 at

TABLE I. Properties of materials included in the FEA simulation of the x-ray heated DAC. k, thermal conductivity; ρ, density; cp, specific heat capacity; μ, x-ray attenuation coefficient.

	Diamond	Re	Fe	KCl
k [W/m/K]	990	48	50	20
ρ [kg/m^3]	3515	21020	13000	5000
cp [J/kg/K]	520	140	700	690
μ [1/m]	158		43000	2513

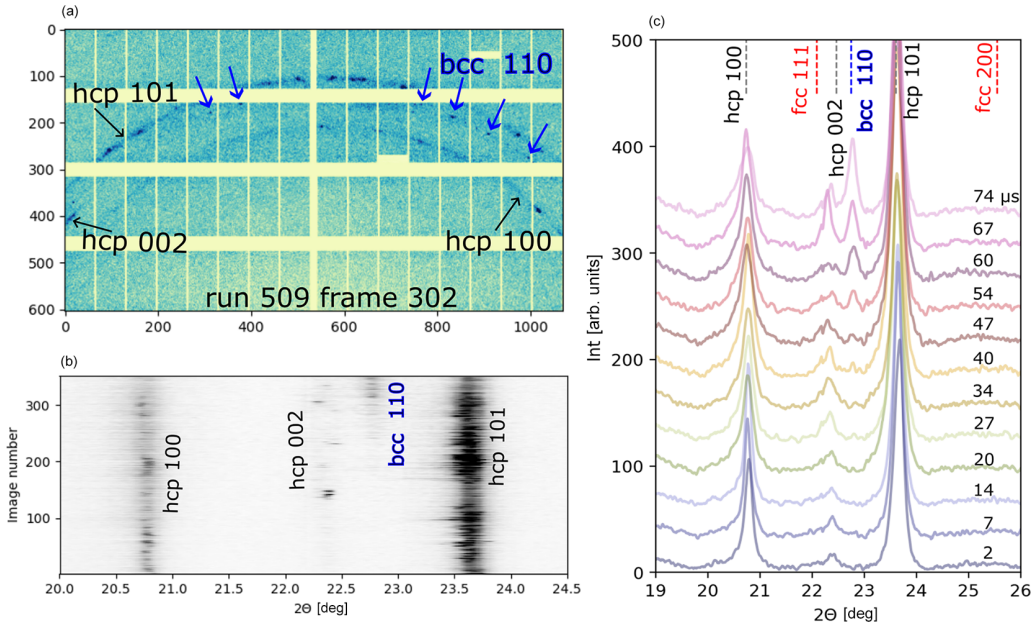

FIG. 2. Data from the CC273 DAC showing the first pulse train that transforms part of the sample into the cubic structure at 30-40 μJ of pulse energy. (a) A raw diffraction image from pulse 302 shows 110 bcc-Fe spots (blue arrows). (b) Stacked integrated patterns (bottom to top in time) reveal a new reflection near the end of the pulse train, as hcp-Fe peaks fade. (c) 2θ-intensity plots, averaged over 10 pulses every 30 (e.g., 1–10, 30–40, etc.), show the emergence of the 110 bcc-Fe reflection; patterns are vertically offset. In red is shown theoretical position of fcc peaks with the same unit cell volume as the hcp and bcc structures (15 Å^3).

pressures between 10 and 138 GPa, progressively decreasing x-ray attenuation at various pressures [33]. The previously published phase diagram of Fe was reproduced correctly, after developing a proper data processing technique and metrology (see details in Ref. [33]). We then moved on to investigate Fe at more elevated pressures. First, a single, highly attenuated x-ray pulse train was used to probe the sample without significantly increasing its temperature [Fig. 1(b), top panel]. Within each train, the x-ray pulse intensity increased progressively toward the end of the train [Fig. 1(c), bottom panel], enabling the sample to be probed initially in its cold state or after only slight annealing. At this stage, only two hcp-Fe reflections were visible: the 100 and 101 peaks [Fig. 1(b), top panel].

For each sample, multiple runs were acquired while incrementally increasing the x-ray beam transmission (typically in steps of 0.5% or 1%), with the sample repeatedly probed at the same location [Fig. 1(b)]. Figure 1(c) shows the evolution of the sample through the position of the hcp-Fe 101 reflection over a series of pulse trains with increasing average intensity. Following the first few pulse trains, the 2θ positions of the Fe reflections shifted to lower angles, indicating annealing of the sample caused by elevated temperatures reached during the preceding trains.

The first weakly attenuated pulse train (run 500 for CC273 and run 548 for HIBEF38) produced negligible heating toward the end of the train, whereas more substantial heating was observed in the subsequent trains (run 505 for CC273 and run 550 for HIBEF38), as evidenced by the first appearance of the hcp-Fe 002 reflection [Fig. 1(b)]. In later, higher-power trains, additional 002 Bragg reflections appeared and the position of the hcp-Fe 101 reflection no longer shifted toward lower 2θ values despite further increases in x-ray pulse energy [Figs. 1(b) and 1(c)].

The initial low-intensity pulse trains produced diffraction patterns containing only the hcp-Fe 100, 002, and 101 reflections, consistent with the detector coverage. As the x-ray pulse intensity increased throughout each train, the corresponding rise in temperature was manifested by a shift of the diffraction peaks toward lower diffraction angles, reflecting thermal expansion of the crystal lattice.

A. Samples at pressures exceeding 200 GPa

1. X-ray diffraction observations

At high temperatures, the behavior differs markedly between the two samples with the highest initial pressures (208 GPa for HIBEF38, runs 517–562, and 218 GPa for CC273, runs 498–516) and the three samples at lower pressures (122–152 GPa). We first focus on the two highest-pressure samples.

As the pulse-train intensity was increased, a distinct additional diffraction peak appeared between the positions of the hcp-Fe 002 and 101 reflections during the final third of the pulse train (Fig. 2 and Fig. 3; Movie 1 in the Supplemental Material). This peak is absent in the cold starting material and is not observed after quenching to ambient temperature. Apart from this new feature, all observed diffraction peaks can be attributed to the starting components of the DAC sample chamber: hcp-Re, bcc-KCl, and hcp-Fe—while the diffraction peaks from Re and KCl are nearly indistinguishable from the background.

Potential contaminants, such as iron carbides (e.g., Fe_3C [9,27,28]), can be ruled out because their diffraction

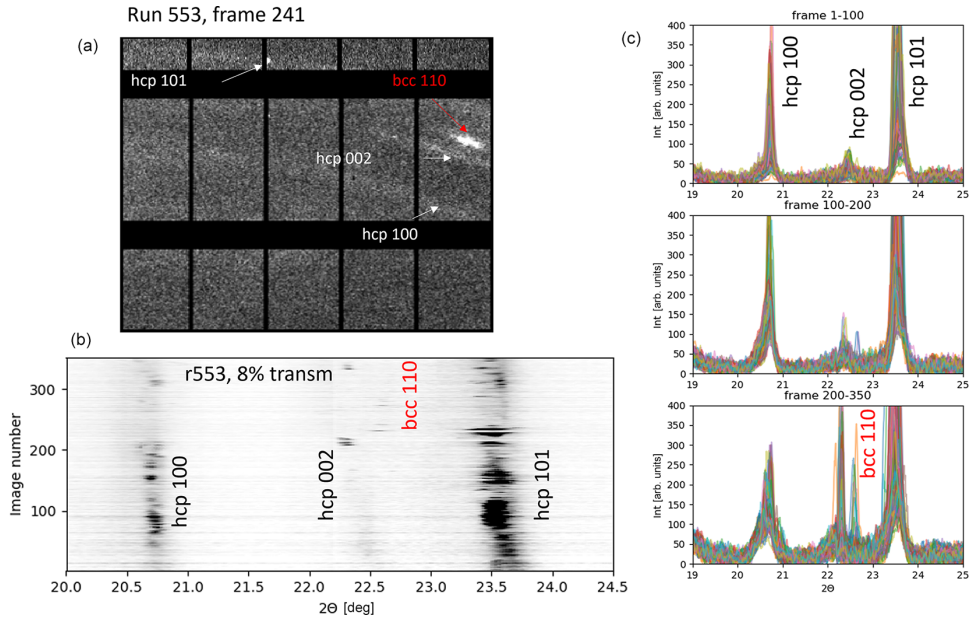

FIG. 3. Data from the HIBEF38 DAC. Run 553 is the first train on this sample that transforms part of the sample into the cubic structure at 40–50 μJ of pulse energy. (a) Focus on part of the raw image showing a bcc reflection in similar orientation to the 002 hcp peak, hinting at the microstructural signature of a martensitic transformation. (b) Stacked integrated diffraction patterns from all 352 pulses showing a bcc reflection in the last part of the pulse train (time from bottom-up), at the same time as diminishing of all hcp-Fe peaks. (c) 2θ vs intensity plots of the integrated patterns from the first 100 pulses (top), 100–200 pulses (center), and 200–350 pulses (bottom) showing the emerging 110 bcc-Fe reflection.

patterns differ substantially from the observed data. Furthermore, the additional reflection between the positions of the hcp-Fe 002 and 101 reflections disappears upon quenching from high temperature, in contrast to the behavior expected for a phase produced by a chemical reaction. The possibility of reaction-induced phase formation is further limited by the short cumulative heating time prior to the transition, which remained well below 1 ms over all pulse trains.

The individual Bragg reflections of the new phase exhibit first intense single-crystal-like spots and later in the train a powder component. As the transformation progresses, the number and intensity of the new reflections increase, while the average intensity of all three hcp-Fe reflections decreases, indicating that the new phase forms through a bulk transformation of the iron foil (Figs. 2 and 3).

Because only a single new reflection is observed across the entire measured 2θ range, the most plausible crystal structure is one with high symmetry. Indexing this reflection as the fcc 111 peak yields a volume that is approximately 7% lower than that of hcp Fe at ambient temperature, an implausibly large difference [37]. Moreover, the second fcc reflection (200), which lies within the accessible diffraction range, is never observed. Structures with lower symmetry than cubic would be expected to produce additional reflections within the measured 2θ range, yet no such peaks are detected.

Consequently, indexing the new reflection as the bcc 110 peak provides the only physically plausible solution. This assignment yields a volume that is approximately 1.3% larger than that of hcp Fe at 300 K and is consistent with the observed number of reflections, as the next bcc reflection (200) falls outside the detector coverage. The volumes of the coexisting hcp and bcc phases are nearly identical at the transformation temperature, indicating similar densities (Fig. 4).

The data are consistent with a small but positive volume change accompanying the hcp-to-bcc transformation. Accord-

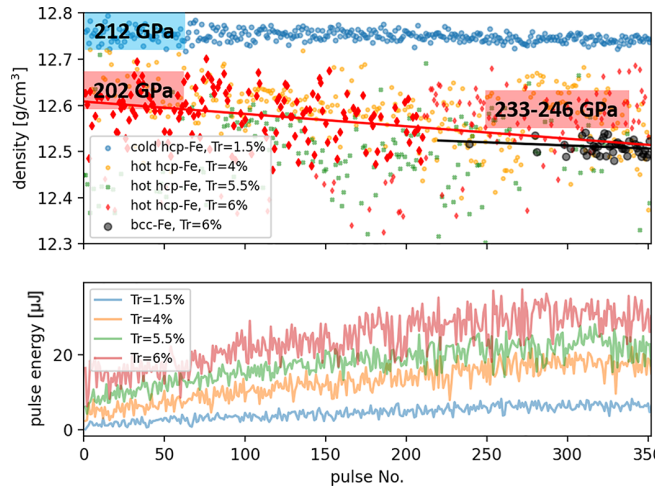

FIG. 4. Calculated densities of hcp and bcc phases. Data are from runs 500 (1.5% transmission), 505 (4%), 508 (5.5%), and 509 (6%) (sample CC273, top panel) with increasing pulse energies (bottom panel), demonstrating that the volume change between the hcp and bcc structures is small but positive. In red is the first run in the series with the bcc structure. Red and black lines are linear regressions to hcp and bcc densities, respectively. "Tr" indicates x-ray transmission. The pressures were calculated from equation of state by Dewaele *et al.* [32], Table II.

TABLE II. Pressure calculation. Pressures were calculated from the thermal equation of state of Dewaele *et al.* [32] for hcp-Fe based on measured volumes from the HIBEF38 cell, run 553 (top) and CC273 cell, run 509 (bottom). Temperatures between 4000 K and 5000 K are considered.

V0	V	T [K]	P [GPa]
14.6		300	209
	15.0	4000	221
	15.0	5000	233
14.7		300	202
	14.8	4000	233
	14.8	5000	246

ing to the Clapeyron relation, $dT/dP = \Delta V/\Delta S$, this implies a zero or positive Clapeyron slope for the hcp–bcc phase boundary. A positive Clapeyron slope would indicate that the temperature required to stabilize the bcc phase increases with pressure.

2. *Streaked optical pyrometry temperatures*

The average temperature during the portion of the x-ray pulse train for which thermal emission becomes detectable and the bcc phase is observed (i.e., approximately the last third of the pulse train) is estimated to be 4400(500) K based on optical pyrometry measurements [31] (Fig. 5).

In addition to thermal emission from the hotspot, fluorescence from the sample, pressure-transmitting medium (PTM), and diamond anvils is commonly observed. The fluorescence signal typically increases approximately linearly with the total x-ray power, whereas the thermal emission is expected to increase much more rapidly because of its strong dependence on temperature [31].

For HIBEF38, runs up to 551 are assumed to be dominated by fluorescence from the diamond anvils, while the onset of detectable thermal emission occurs in runs 552 and 553. Run 551 was therefore used as a background image and subtracted from run 553 to correct for the fluorescence contribution. Averaging the signal over the final third of the pulse train yields a temperature of 4382 ± 70 K from a fit of the Planck function over the wavelength range 550–780 nm (Fig. 5). Accounting for additional sources of uncertainty, including the sensitivity of the fit to the selected spectral range and possible temperature variations during the pulse train, we estimate the overall temperature uncertainty to be ±500 K.

3. *Finite element analysis*

The temperatures obtained from the FEA simulations were calibrated against the experimentally measured temperatures by matching the spatiotemporal average temperature of the sample surface during the final third of the pulse train. This calibration was achieved by applying a scaling factor to the input pulse energies to account for uncertainties in the absolute pulse-energy measurements and deviations of the x-ray beam profile from an ideal Gaussian distribution.

The FEA simulations indicate that the highest temperatures occur at the center of the sample, which undergoes repeated heating and cooling cycles throughout the pulse train, with the amplitude of the temperature oscillations increasing with the average temperature (Fig. 6). Importantly, each x-ray diffraction (XRD) snapshot is acquired at the minimum temperature of the cycle, following cooling from the peak temperature reached after the preceding pulse. At the x-ray intensities for which the new diffraction peak is observed, the temperature may decrease by as much as 2000 K between the peak of the heating cycle and the subsequent XRD measurement (Fig. 6).

Given an average temperature of approximately 4400 K, as measured by SOP on the sample surface during the final stage of the pulse train, the simulations suggest that peak temperatures likely exceeded 6000 K. Such temperatures are sufficient to induce partial melting and subsequent recrystallization, considering that the melting temperature of iron at 230 GPa is estimated to be approximately 5300 K [10].

B. Samples at lower pressures (120–160 GPa)

Samples investigated at lower pressures (122–152 GPa initial pressure) exhibit more complex behavior. At elevated temperatures, the diffraction patterns are dominated by intense diffuse streaks connecting the hcp-Fe 100 and 101 reflections [Fig. 7(b), Supplemental Movie 2], a feature commonly associated with stacking faults in the hcp–fcc system and previously observed during conventional laser-heating

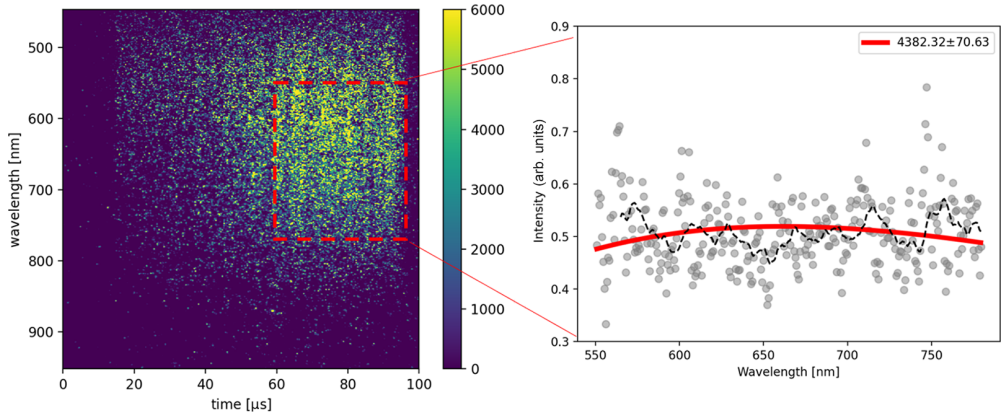

FIG. 5. Spectrally resolved streak optical pyrometry (SOP) for HIBEF38, run 553. A raw streak image (left) and temperature fit to emission data averaged over a 60–95 μs time window (right).

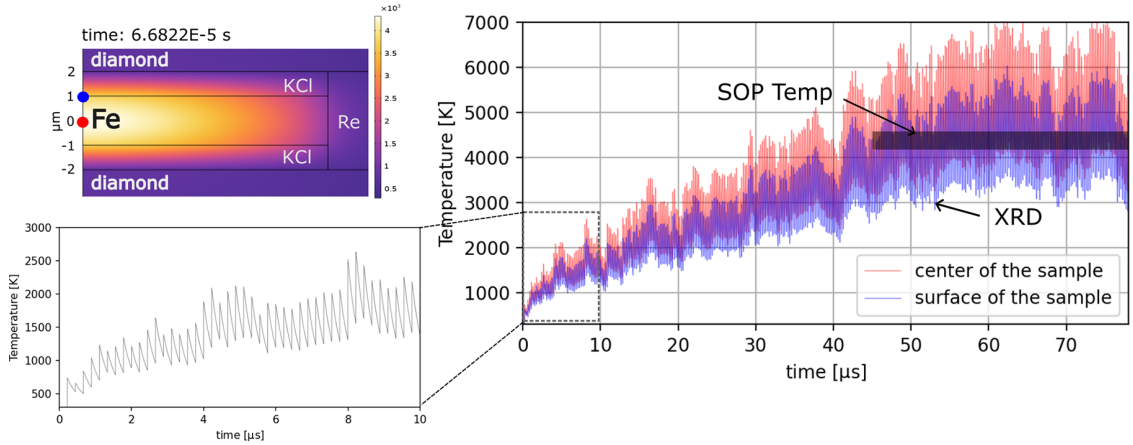

FIG. 6. Finite-element analysis of the spatial and temporal temperature distribution in the sample. The inset shows the temperature evolution at the sample center during the first 10 μs of the pulse train, illustrating the cyclic heating induced by x-ray pulse absorption and the subsequent cooling by thermal conduction. The temperature rises rapidly following each x-ray pulse and decreases during the 222 ns interval before the arrival of the next pulse. The x-ray diffraction measurements probe the sample during this cooling period following each pulse. The dark gray region in the right panel indicates the time window over which the temperature is determined using SOP (see Fig. 5).

experiments [25]. In addition, we observe incipient nucleation of the bcc phase, evidenced by diffuse speckles and sporadic bcc reflections [Figs. 7(a) and 7(c)]. However, these reflections persist for only a few microseconds and never develop into a powderlike diffraction ring. The corresponding temperatures are relatively low (approximately 2000 K) and are unlikely to approach melting conditions.

In contrast, at the highest temperatures reached near the end of the pulse train, the fcc 111 reflection—and occasionally the 200 reflection—appears (Fig. 8). The 111 reflection develops into a textured powder diffraction line, whereas the weak and often absent 200 reflection is consistent with observations reported at lower pressures (P1 cell, 80 GPa; Fig. 4 in [33]). The measured fcc unit-cell volume of 32.113 Å^3 is substantially smaller than the final fcc volume reported by Anzellini *et al*. along the iron melting curve (35.969 Å^3) [10]. This observation suggests that, under the thermodynamic conditions explored here, the hcp–fcc–liquid triple point occurs at significantly higher pressures than previously proposed.

Overall, these observations indicate strong competition among the hcp, bcc, and fcc phases within this pressure range. Unlike in samples compressed above 200 GPa, the bcc phase remains transient and does not evolve into a fully developed crystalline phase.

IV. DISCUSSION

A. On the high pressure phase diagram of Fe

Our observations are summarized in Fig. 9, together with selected results from previous studies for comparison. The phase diagram proposed by Anzellini *et al*. [10], based on diamond anvil cell (DAC) experiments, established the melting curve of iron but did not extend into the pressure-temperature region where the bcc phase is observed in the present study. To date, stabilization of the bcc phase at high pressure and temperature has been predicted primarily by theoretical studies, notably those of Belonoshko and co-workers (e.g., Ref. [18]).

Another high-pressure DAC study by Tateno *et al*. [9] reached comparable pressures but not sufficiently high temperatures and reported only the hcp phase of iron. More recently, dynamic-compression XAS experiments by Balugani *et al*. [21] explored Hugoniot states that approach the pressure-temperature conditions investigated here; however, no phase transition was identified from their indirect measurements.

A more comprehensive comparison with previous studies, based on the phase diagram of Fe compiled by Singh [5], is provided in the Supplemental Material [38] (Fig. S11).

B. Microstructure and potential formation mechanism

At pressures above 200 GPa, the bcc structure is unambiguously observed as a polycrystalline phase at high temperatures below the melting point during cooling from a transiently molten state. This suggests that the growth of bcc crystallites is facilitated by solidification from the melt. In contrast, below 180 GPa, our observations point to a markedly different regime in which metastable bcc crystallite formation competes with thermally disordered close-packed phases at elevated temperatures, the latter also being reported previously [25,37].

The time-resolved nature of the experiment allows us to observe the formation of the first bcc grains as the temperature gradually increases on average from pulse to pulse (Fig. 10). Initially, isolated diffuse speckles appear about 31 μs into the train at the 2θ angle between the 002 and 101 hcp peaks [Figs. 10(a)–10(d)]. The temperature at the probing moment is about 3000 K. As the pulse train progresses, these broad speckles evolve into more localized sharper spots and shift to a slightly smaller 2θ angle (3500–4500 K, 37–43 μs). Up to this point, the temperature oscillations should remain below the melting point of iron at this pressure, approximately 5200 K. At the end of the train (55–77 μs, 5000 K), very sharp, bright Bragg spots form with a random distribution along the azimuthal angle forming a powderlike diffraction ring [Fig. 10(f)]. During this time, the maximum temperatures most likely exceed the melting line.

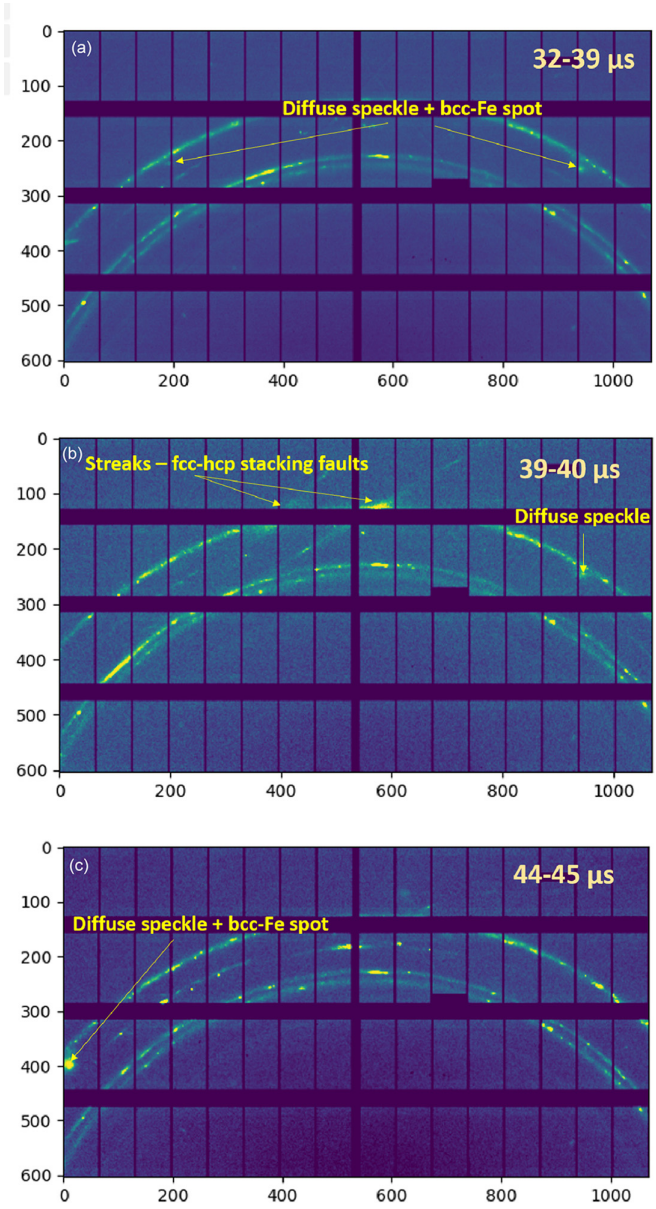

FIG. 7. Data from BetsaA sample, starting pressure 152 GPa, run 452, 7% x-ray transmission (up to 40–45 μJ pulse energy), showing transient states of bcc stacking fault structures. (a) Raw image averaged over frames 144–176 shows diffuse speckles with central Bragg spots. (b) Averaged image over frames 176–181 with clear diffraction streaks due to fcc-hcp stacking faults. Diffuse speckle is here also visible on the right. (c) Average image over frames 197–203 in the bottom panel shows an intense bcc-Fe reflection that disappears after 1 μs.

During the initial stage of the transformation [Figs. 10(a)–10(d) and 3], microstructural features indicative of a displacive (martensitic) phase transition are observed. In particular, the hcp 002 peaks appear in angular proximity to the bcc 110 peak, consistent with the well-established orientation relationship in the Burgers mechanism where these dense atomic planes are parallel. Such a martensitic transformation pathway has been experimentally observed in the bcc–hcp transition of Fe at 14 GPa [39]. The Burgers mechanism

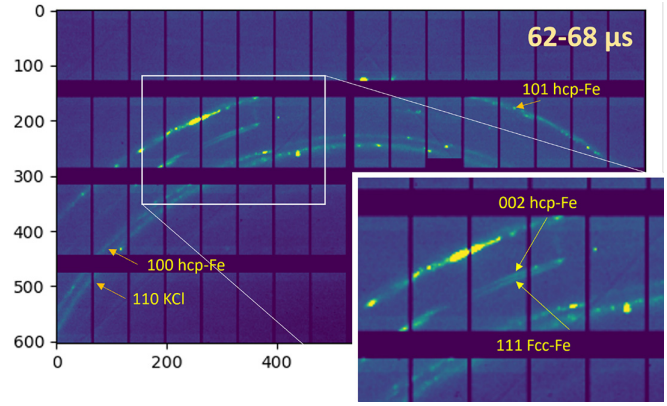

FIG. 8. Continuation of the data from run 452 (BetsaA sample, starting pressure 152 GPa). fcc structure of iron is observed at much higher pressures than previously reported.

has also been numerically induced by molecular dynamics for the hcp-bcc transition in Mg [40]. In this study it is found that the growth of the bcc phase is facilitated by the formation of lamellar nanotwins oriented along the hcp *c* axis, which efficiently accommodates the transformation-induced shear strain. The simulations further reveal a small volume change during the progression from nucleus formation to nanotwin growth, which may explain the initially variable 2θ positions of the bcc-Fe 110 reflections observed in our data [Figs. 10(b)–10(d)]. Subsequent detwinning, potentially assisted by partial melting, leads to the formation of

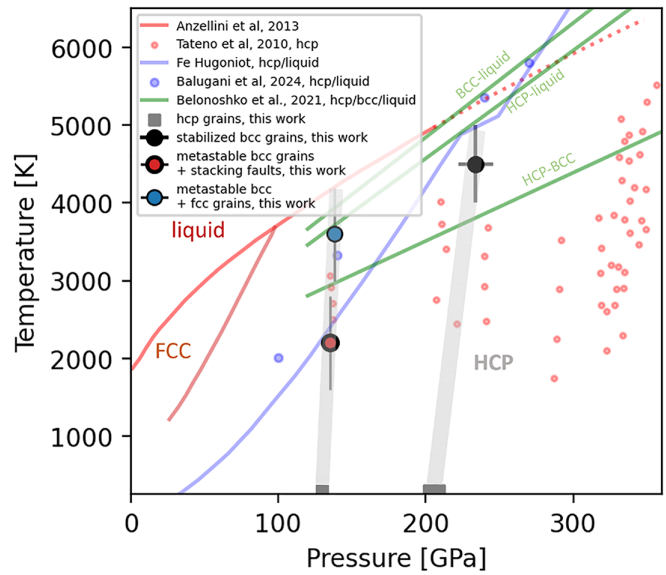

FIG. 9. Experimental data (circles) are colored by observed structure: black (stabilized bcc grains), dark blue (fcc grains), dark red (stacking faults in hcp/fcc), and gray (pure hcp, always present). The black contours around the red and blue dots represent presence of metastable bcc grains. Laser-heated DAC results are in red: bright red lines show the melting curve and fcc stability from Anzellini *et al.* [10]; red circles show the observation of stable hcp-Fe from Tateno *et al.* [9]. Molecular dynamics phase boundaries from Belonoshko *et al.* [18] are in green. Shock compression data are in blue: line—Fe Hugoniot [1]; circles—hcp/liquid Fe from Balugani *et al.* [21].

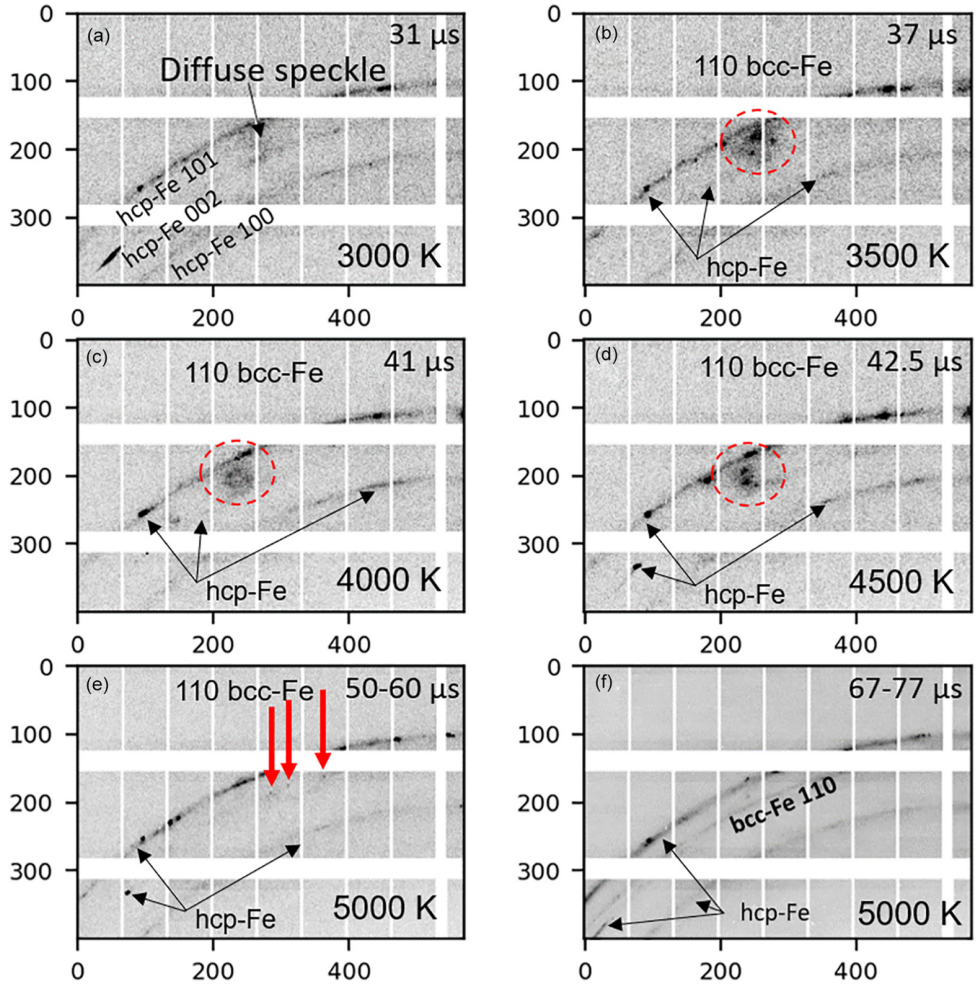

FIG. 10. Evolution of diffuse speckles to the powderlike ring of 110 bcc-Fe reflection with time. Sample CC273, Run 509, 218 GPa. (a) Diffuse speckles of bcc-Fe appear ∼30 μs into the run, between the 002 and 101 diffraction lines of hcp-Fe. (b)–(e) bcc speckles evolve into more localized, sharper spots and shift in azimuth and towards a slightly smaller 2θ between ∼30 and ∼60 μs. (f) Later in the run, bcc-Fe is fully crystallized and forms a continuous powder diffraction ring.

polycrystalline bcc Fe, as evidenced by the emergence of multiple randomly oriented diffraction spots in the final stages of the transformation.

C. Differences with previous studies

An important question arises as to why this long-sought-after phase has not been observed in previous experimental studies on iron. In the following, we discuss the key differences between our experiments and previous studies and propose potential explanations, which may stem from differences in the experimental approach or the underlying nature of phase stability.

1. Thermodynamical pathway

One possible factor may relate to the distinct thermodynamic pathways imposed in the present study, namely the nucleation processes that may favor other than thermodynamically stable phases [41,42]. The MHz heating and cooling cycles used to generate extreme temperatures in our study result in cooling rates of ∼10 K/ns when temperatures exceed 4000 K. Molecular dynamics calculations of rapid solidification of liquid copper at comparable cooling rates (100 K/ns) have shown that metastable high temperature phases can be formed at the interface between the liquid and the nucleating solid phase as this configuration reduces the free energy of the interface [42]. The polymorphic solidification observed in their study matches our findings: below a certain pressure (in our study below 180 GPa), small body-centered cubic nuclei (bcc) and close-packed nuclei form, but the bcc nuclei quickly transform into close-packed phases (fcc, hcp), while above this pressure (200 GPa in our study), nucleation starts in the bcc phase and grows, suggesting that the solidification process stabilizes the metastable bcc phase. Such kinetically stabilized phase regions for iron implied by our experimental observations are depicted in Fig. 9: the red circle marks conditions where unstable bcc nucleation competes with the formation of hcp/fcc stacking faults at lower temperatures, while fcc growth is favored at higher temperatures (blue circle). At higher pressures (black circle), the final powder texture of the bcc phase appearing in many consecutive XRD images above 230 GPa suggests that a narrow stability field of the bcc phase is reached. Its presence on our accessible timescales (tens of microseconds) is unambiguous.

However, our data do not allow us to conclusively determine whether the observed transformation is governed by kinetic or thermodynamic factors.

Compared to standard laser heated (LH) DAC experiments, our methodology offers significant advantages in detecting new phases. The high rate of diffraction data (352 XRD patterns in 78 μs) and high brilliance monochromatic source coupled to novel volumetric heating enable unambiguous detection of structural intermediary states and conditions directly adjacent to melting. The rapid dynamics of nucleation could be challenging to observe in synchrotron XRD experiments. The volumetric absorption of the x-ray energy helps transform a larger sample volume in the center of the foil, even as the surface remains close to the cool diamond interface, particularly at extreme pressures. In addition, x-ray heating experiments always probe high temperature states upon cooling and therefore access different thermodynamic pathways from most conventional LH DAC and laser compression experiments which study phase transitions upon heating [4–6,9,10].

2. X-ray heating

An additional key distinction between our experiments and previous studies lies in the nature of heating. In our case, heating is induced by intense, short-pulse hard x-ray irradiation at power densities of 10^{15}–10^{16} W/cm^2. This regime enables direct core-electron excitation, leading to extremely high electron temperatures within the first few picoseconds. Rapid rise in electron temperature can drive nonthermal phase transitions by altering ionic potentials before significant lattice heating occurs. For example, in iron at ambient pressure, theoretical studies predict that a solid-solid phase transition from the bcc to the fcc structure can be induced under high electron temperatures, even when the lattice remains near room temperature [43]. However, a crucial question remains: can a phase transition initiated under such extreme electronic conditions persist over longer timescales, particularly after electron-ion energy equilibration? Transient electronic excitations last for picoseconds at most after x-ray exposure and the structural dynamics observed here persist on the timescale of microseconds. Still, these effects might be relevant in cases where the Gibbs free energies of competing high-pressure phases are similar, making their stability potentially sensitive to transient electronic effects [20].

D. Geoscience implications

Our results place the formation of the bcc structure in the range of 233–246 GPa and 4000–5000 K, based on the measured hcp-Fe volumes and the thermal equation of state of Fe [32] (Fig. 9, Table II). If the cubic phase is indeed stable, it has major implications for the structure of Earth's solid inner core—affecting its melting temperature, the partitioning of light elements during crystallization, and seismic anisotropy. Most *ab initio* studies on element partitioning assume that hcp-Fe is stable under inner core conditions [44,45] and experimental studies do not reach the bcc stability field observed here [46–48]. Similarly, elasticity measurements used to infer core composition have focused mainly on hcp alloys [49–52]. Stabilization of a different phase at these conditions thus may challenge existing compositional models of the Earth's inner and outer core, which should be the topic of further studies.

V. CONCLUSIONS

This work investigated the phase diagram of Fe near its melting boundary using intense MHz-rate x-ray pulses from the European X-ray Free-Electron Laser at pressures exceeding 200 GPa.

Our experimental approach differs fundamentally from previous studies of the high-pressure/high-temperature phase diagram of Fe in several respects. First, heating occurs over a relatively short timescale, with 352 x-ray pulses separated by 222 ns delivered within an 80 μs pulse train. Second, time-resolved x-ray diffraction probes the structural evolution as the sample cools from temperatures reaching up to ∼2000 K above the probing temperature, implying that the observed high-temperature phases reflect the crystallization pathway from a transient molten state. Third, heating is initiated through intense femtosecond hard x-ray irradiation, which initially drives the electronic subsystem far from equilibrium before energy is transferred to the lattice.

Within the 120–160 GPa pressure range, the high temporal resolution of the measurements reveals the persistence of fcc Fe beyond its previously established stability field. Transient intermediate structures, including bcc Fe and stacking-fault-rich configurations, are also observed, providing direct insight into the transformation pathway during rapid cooling. At pressures above 230 GPa, new diffraction reflections appear at high temperature, indicating the nucleation of a previously unreported phase that subsequently evolves into a powderlike diffraction pattern consistent with bcc Fe.

These observations provide direct experimental evidence for the formation of the long-sought bcc phase of Fe at pressures exceeding 200 GPa and reveal the kinetic pathway through which it forms. The present work demonstrates the capability of MHz-rate XFEL to create and capture transient structural states during phase transformations. This approach opens up opportunities for investigating metastable phases and crystallization pathways in materials subjected to extreme pressure and temperature conditions.

ACKNOWLEDGMENTS

The authors are indebted to the HIBEF user consortium for the provision of instrumentation and staff that enabled this experiment. We acknowledge European XFEL in Schenefeld, Germany, for provision of x-ray free-electron laser beamtime at Scientific Instrument HED (High Energy Density Science) and would like to thank the staff for their assistance. We acknowledge DESY (Hamburg, Germany), a member of the Helmholtz Association HGF, for the provision of experimental facilities. Parts of this research were carried out at PETRA III (beamline P02.2). The authors also wish to thank S. Chariton for assistance during beamtime. The authors wish to thank S. Vitale for technical assistance with Focused Ion Beam milling at Earth & Planets Laboratory. We thank H. P. Liermann, T. Michelat, P. Schmidt, and J. Moore for their support. D.A. and S.B. have received funding from the European Research Council (ERC) under the European Union's Horizon 2020 research and innovation

programme (Grant Agreement No. 724690). H.M. and E.K. were supported by European Union's Horizon 2020 research and innovation programme (ERC Grant No. 864877) and UKRI STFC Grant No. ST/V000527/1. R.S.M., B.M., and Z.Y. were supported by the ERC under the European Union's Horizon 2020 research and innovation programme (Grant Agreement No. 101002868) and RCUK-EPSRC Grant No. EP/P024513/1. S.M., J.C., and H.G. are funded by the European Union (ERC, HotCores, Grant No. 101054994). K.A. received support from DFG Grant No. AP262/2-2 and K.B. received funds from DFG Project No. AP262/2-2. This work was supported by Grant No. EP/S022155/1 (M.I.M., M.J.D.) from the UK Engineering and Physical Sciences Research Council. J.D.M. is grateful to AWE for the award of CASE Studentship No. P030463429. O.B.B. acknowledges the support of the Scottish Doctoral Training Program in Condensed Matter Physics (CM-CDT). G.M. and N.J. were supported by ANR grant MinDIXI (No. ANR-22-CE49-0006) and Labex OSUG@2020 (Investissements d'avenir—ANR10 LABX56) and IDEX Université Grenoble Alpes. L.E., A.S.M., and T.X. were supported by NASA–Solar-System-Workings program under Grant No. 80NSSC17K0765. A.F.G. and E.E. were supported by U.S. National Science Foundation Grants No. EAR-2049127, No. CHE-2302437, and Carnegie Science. Part of this work was performed under the auspices of the U.S. Department of Energy by Lawrence Livermore National Laboratory under Contract No. DE-AC52-07NA27344 (H.C.). V.P. was supported by the National Science Foundation-Earth Sciences (Grant No. EAR-658 1634415).

Views and opinions expressed are however those of the author(s) only and do not necessarily reflect those of the European Union or the European Research Council. Neither the European Union nor the granting authority can be held responsible for them.

Conceptualization: Z.K., E.E., H.C., H.M., C.P., R.S.M., G.M., and S.M. Methodology: Z.K., N.J., C.S., K.A., H.G., T.L., H.M., M.I.M., J.S., C.P., R.S.M., G.M., and S.M. Software: Z.K., O.B.B., and C.P. Validation: Z.K., H.G., N.J., C.S., C.P., R.S.M., G.M., and S.M. Formal analysis: Z.K., E.E., A.D., H.G., N.J., E.K., V.P., R.S.M., and S.M. Investigation: Z.K., E.E., A.D., R.J.H., N.J., C.S., A.S.M., K.A., M.B., S.B., K.B., J.C., A.P.D., L.E., K.G., E.K., B.M., J.D.M., M.I.M., V.P., M.T, T.X., Z.Y., A.F.G., R.S.M., and S.M. Resources: Z.K., A.D., C.S., D.A., L.E., E.K., H.M., M.I.M., A.F.G., R.S.M., and S.M. Data curation: Z.K., E.E., N.J., A.F.G., C.P., G.M., and S.M. Writing–original draft: Z.K., E.E., and G.M. Writing–review and editing: Z.K., E.E., A.D., N.J., C.S., D.A., S.B., H.C., H.M., B.M., J.D.M., M.I.M., Z.Y., A.F.G., C.P., R.S.M., G.M., and S.M. Visualization: Z.K., E.E., and A.D. Supervision: Z.K., E.E., C.S., H.M., A.F.G., R.S.M., G.M., and S.M. Project administration: Z.K., H.M., U.Z., A.F.G., C.P., G.M., and S.M. Funding acquisition: D.A., K.A., H.M., U.Z., A.F.G., R.S.M., and S.M.

DATA AVAILABILITY

All data used in this paper were collected at the High Energy Density (HED) beamline of the European X-ray Free Electron Laser (EuXFEL) during the #3063 community proposal, with additional characterization during pre- and post-screening times at the P02.2 beamline of the PETRA III synchrotron. The original European XFEL data is located at [53]. Additional source data and intermediate data processing results are on Zenodo [54].

[1] J. M. Brown and R. G. McQueen, Phase transitions, grüneisen parameter, and elasticity for shocked iron between 77 GPa and 400 GPa, J. Geophys. Res.: Solid Earth **91**, 7485 (1986).

[2] J. H. Nguyen and N. C. Holmes, Melting of iron at the physical conditions of the Earth's core, Nature (London) **427**, 339 (2004).

[3] Y. Zhang, Y. Wang, Y. Huang, J. Wang, Z. Liang, L. Hao, Z. Gao, J. Li, Q. Wu, H. Zhang, Y. Liu, J. Sun, and J.-F. Lin, Collective motion in hcp-Fe at Earth's inner core conditions, Proc. Natl. Acad. Sci. USA **120**, e2309952120 (2023).

[4] S. J. Turneaure, S. M. Sharma, and Y. M. Gupta, Crystal structure and melting of Fe shock compressed to 273 GPa: In situ x-ray diffraction, Phys. Rev. Lett. **125**, 215702 (2020).

[5] S. Singh, R. Briggs, M. G. Gorman, L. X. Benedict, C. J. Wu, S. Hamel, A. L. Coleman, F. Coppari, A. Fernandez-Pañella, C. McGuire, M. Sims, J. K. Wicks, J. H. Eggert, D. E. Fratanduono, and R. F. Smith, Structural study of hcp and liquid iron under shock compression up to 275 GPa, Phys. Rev. B **108**, 184104 (2023).

[6] S. White, B. Kettle, J. Vorberger, C. L. S. Lewis, S. H. Glenzer, E. Gamboa, B. Nagler, F. Tavella, H. J. Lee, C. D. Murphy, D. O. Gericke, and D. Riley, Time-dependent effects in melting and phase change for laser-shocked iron, Phys. Rev. Res. **2**, 033366 (2020).

[7] Y. Ping, F. Coppari, D. G. Hicks, B. Yaakobi, D. E. Fratanduono, S. Hamel, J. H. Eggert, J. R. Rygg, R. F. Smith, D. C. Swift, D. G. Braun, T. R. Boehly, and G. W. Collins, Solid iron compressed up to 560 GPa, Phys. Rev. Lett. **111**, 065501 (2013).

[8] R. G. Kraus, R. J. Hemley, S. J. Ali, J. L. Belof, L. X. Benedict, J. Bernier, D. Braun, R. E. Cohen, G. W. Collins, F. Coppari, M. P. Desjarlais, D. Fratanduono, S. Hamel, A. Krygier, A. Lazicki, J. Mcnaney, M. Millot, P. C. Myint, M. G. Newman, J. R. Rygg, *et al.*, Measuring the melting curve of iron at super-Earth core conditions, Science **375**, 202 (2022).

[9] S. Tateno, K. Hirose, Y. Ohishi, and Y. Tatsumi, The structure of iron in Earth's inner core, Science **330**, 359 (2010).

[10] S. Anzellini, A. Dewaele, M. Mezouar, P. Loubeyre, and G. Morard, Melting of iron at Earth's inner core boundary based on fast x-ray diffraction, Science **340**, 464 (2013).

[11] L. Stixrude and R. E. Cohen, Constraints on the crystalline structure of the inner core: Mechanical instability of bcc iron at high pressure, Geophys. Res. Lett. **22**, 125 (1995).

[12] L. Stixrude, Structure of iron to 1 Gbar and 40 000 K, Phys. Rev. Lett. **108**, 055505 (2012).

[13] A. B. Belonoshko, T. Lukinov, J. Fu, J. Zhao, S. Davis, and S. I. Simak, Stabilization of body-centred cubic iron under inner-core conditions, Nat. Geosci. **10**, 312 (2017).

[14] Y. Sun, M. I. Mendelev, F. Zhang, X. Liu, B. Da, C.-Z. Wang, R. M. Wentzcovitch, and K.-M. Ho, *Ab initio* melting temperatures of bcc and hcp iron under the Earth's inner core condition, Geophys. Res. Lett. **50**, e2022GL102447 (2023).

[15] L. Vočadlo, D. Alfe, M. J. Gillan, I. G. Wood, J. P. Brodholt, and G. D. Price, Possible thermal and chemical stabilization of body-centred-cubic iron in the Earth's core, Nature (London) **424**, 536 (2003).

[16] L. Zhao, V. Lordi, and A. Samanta, Melting point of iron at high pressure: An assessment of uncertainties and effect of electronic temperature, Appl. Phys. Lett. **124**, 144105 (2024).

[17] A. B. Belonoshko, R. Ahuja, and B. Johansson, Stability of the body-centred-cubic phase of iron in the Earth's inner core, Nature (London) **424**, 1032 (2003).

[18] A. B. Belonoshko, J. Fu, and G. Smirnov, Free energies of iron phases at high pressure and temperature: Molecular dynamics study, Phys. Rev. B **104**, 104103 (2021).

[19] Z. Li and S. Scandolo, Competing phases of iron at Earth's core conditions from deep-learning-aided *ab-initio* simulations, Geophys. Res. Lett. **51**, e2024GL110357 (2024).

[20] M. Ghosh, S. Zhang, L. Hu, and S. X. Hu, Cooperative diffusion in body-centered cubic iron in Earth and super-Earths' inner core conditions, J. Phys.: Condens. Matter **35**, 154002 (2023).

[21] S. Balugani, J. A. Hernandez, N. Sévelin-Radiguet, O. Mathon, V. Recoules, J. J. Kas, D. E. Eakins, H. Doyle, A. Ravasio, and R. Torchio, New constraints on the melting temperature and phase stability of shocked iron up to 270 GPa probed by ultrafast x-ray absorption spectroscopy, Phys. Rev. Lett. **133**, 254101 (2024).

[22] R. F. Smith, J. H. Eggert, D. C. Swift, J. Wang, T. S. Duffy, D. G. Braun, R. E. Rudd, D. B. Reisman, J. P. Davis, M. D. Knudson, and G. W. Collins, Time-dependence of the alpha to epsilon phase transformation in iron, J. Appl. Phys. **114**, 223507 (2013).

[23] M. G. Gorman, A. L. Coleman, R. Briggs, R. S. McWilliams, D. McGonegle, C. A. Bolme, A. E. Gleason, E. Galtier, H. J. Lee, E. Granados, M. Śliwa, C. Sanloup, S. Rothman, D. E. Fratanduono, R. F. Smith, G. W. Collins, J. H. Eggert, J. S. Wark, and M. I. McMahon, Femtosecond diffraction studies of solid and liquid phase changes in shock-compressed bismuth, Sci. Rep. **8**, 16927 (2018).

[24] Y. Kuwayama, K. Hirose, N. Sata, and Y. Ohishi, Phase relations of iron and iron-nickel alloys up to 300 GPa: Implications for composition and structure of the Earth's inner core, Earth Planet. Sci. Lett. **273**, 379 (2008).

[25] Z. Konôpková, W. Morgenroth, R. Husband, N. Giordano, A. Pakhomova, O. Gutowski, M. Wendt, K. Glazyrin, A. Ehnes, J. T. Delitz, A. F. Goncharov, V. B. Prakapenka, and H.-P. Liermann, Laser heating system at the extreme conditions beamline, P02.2, PETRA III, J. Synchrotron Radiat. **28**, 1747 (2021).

[26] R. Sinmyo, K. Hirose, and Y. Ohishi, Melting curve of iron to 290 GPa determined in a resistance-heated diamond-anvil cell, Earth Planet. Sci. Lett. **510**, 45 (2019).

[27] G. Aprilis, I. Kantor, I. Kupenko, V. Cerantola, A. Pakhomova, I. E. Collings, R. Torchio, T. Fedotenko, S. Chariton, M. Bykov, E. Bykova, E. Koemets, D. M. Vasiukov, C. McCammon, L. Dubrovinsky, and N. Dubrovinskaia, Comparative study of the influence of pulsed and continuous wave laser heating on the mobilization of carbon and its chemical reaction with iron in a diamond anvil cell, J. Appl. Phys. **125**, 095901 (2019).

[28] G. Morard, S. Boccato, A. D. Rosa, S. Anzellini, F. Miozzi, L. Henry, G. Garbarino, M. Mezouar, M. Harmand, F. Guyot, E. Boulard, I. Kantor, T. Irifune, and R. Torchio, Solving controversies on the iron phase diagram under high pressure, Geophys. Res. Lett. **45**, 11074 (2018).

[29] H. P. Liermann, Z. Konôpková, K. Appel, C. Prescher, A. Schropp, V. Cerantola, R. J. Husband, J. D. McHardy, M. I. McMahon, R. S. McWilliams, C. M. Pépin, J. Mainberger, M. Roeper, A. Berghäuser, H. Damker, P. Talkovski, M. Foese, N. Kujala, O. B. Ball, M. A. Baron, *et al.*, Novel experimental setup for megahertz x-ray diffraction in a diamond anvil cell at the High Energy Density (HED) instrument of the European X-ray free-electron laser (EuXFEL), J. Synchrotron Radiat. **28**, 688 (2021).

[30] U. Zastrau, K. Appel, C. Baehtz, O. Baehr, L. Batchelor, A. Berghäuser, M. Banjafar, E. Brambrink, V. Cerantola, T. E. Cowan, H. Damker, S. Dietrich, S. Di Dio Cafiso, J. Dreyer, H.-O. Engel, T. Feldmann, S. Findeisen, M. Foese, D. Fulla-Marsa, S. Göde, *et al.*, The High Energy Density scientific instrument at the European XFEL, J. Synchrotron Radiat. **28**, 1393 (2021).

[31] O. B. Ball, C. Prescher, K. Appel, C. Baehtz, M. A. Baron, R. Briggs, V. Cerantola, J. Chantel, S. Chariton, A. L. Coleman, H. Cynn, H. Damker, D. Dattelbaum, L. E. Dresselhaus-Marais, J. H. Eggert, L. Ehm, W. J. Evans, G. Fiquet, M. Frost, K. Glazyrin, *et al.*, Dynamic optical spectroscopy and pyrometry of static targets under optical and x-ray laser heating at the European XFEL, J. Appl. Phys. **134**, 055901 (2023).

[32] A. Dewaele, P. Loubeyre, F. Occelli, M. Mezouar, P. I. Dorogokupets, and M. Torrent, Quasihydrostatic equation of state of iron above 2 Mbar, Phys. Rev. Lett. **97**, 215504 (2006).

[33] H. Ginestet, R. J. Husband, N. Jaisle, E. Edmund, Z. Konôpková, C. Strohm, M. S. Anae, D. Antonangeli, K. Appel, O. B. Ball, M. Baron, S. Boccato, K. Buakor, J. Chantel, H. Cynn, B. Massani, J. D. Mchardy, M. I. Mcmahon, V. Prakapenka, J. Sztuk-dambietz, *et al.*, Metrology for femtosecond pulsed x-ray heating in diamond anvil cell experiments at the European XFEL: Revisiting the iron phase diagram up to 150 GPa, J. Appl. Phys. **139**, 045901 (2026).

[34] J. Sztuk-Dambietz, V. Rovensky, A. Klujev, T. Laurus, U. Trunk, K. Ahmed, O. Meyer, J. Möller, A. Parenti, N. Raab, R. Shayduk, M. Sikorski, G. Ansaldi, U. Bösenberg, L. M. Luis, A. Muenich, T. R. Preston, P. Schmidt, S. Stern, R. Bean, *et al.*, Operational experience with adaptive gain integrating pixel detectors at European XFEL, Front. Phys. **11**, 1329378 (2024).

[35] J. Meza-Galvez, N. Gomez-Perez, A. S. Marshall, A. L. Coleman, K. Appel, H. P. Liermann, M. I. McMahon, Z. Konôpková, and R. S. McWilliams, Thermomechanical response of thickly tamped targets and diamond anvil cells under pulsed hard x-ray irradiation, J. Appl. Phys. **127**, 195902 (2020).

[36] T. Maltezopoulos, F. Dietrich, W. Freund, U. F. Jastrow, A. Koch, J. Laksman, J. Liu, M. Planas, A. A. Sorokin, K. Tiedtke, and J. Grünert, Operation of X-ray gas monitors at the European XFEL, J. Synchrotron Radiat. **26**, 1045 (2019).

[37] A. S. Mikhaylushkin, S. I. Simak, L. Dubrovinsky, N. Dubrovinskaia, B. Johansson, and I. A. Abrikosov, Pure iron

compressed and heated to extreme conditions, Phys. Rev. Lett. **99**, 165505 (2007).

[38] See Supplemental Material at http://link.aps.org/supplemental/10.1103/kxnf-6c5y for phase diagram summarizing up-to-date experimental and theoretical studies on the melting and structure of pure iron. Caption for movie 1: AGIPD XRD images and corresponding X-ray pulse energy. Movie of 352 2D diffraction images (left) created by X-ray pulses with energies depicted on the right. Data are from run 509, sample CC273, showing formation of bcc Fe at around 230 GPa and 4000-5000 K. Caption for movie 2: AGIPD XRD images and corresponding X-ray pulse energy. Movie of 352 2D diffraction images (left) created by X-ray pulses with energies depicted on the right. Data are from run 452, sample BetsaA, showing stacking faults and diffuse speckles at pressures above 236 GPa and high temperatures.

[39] R. Fréville, A. Dewaele, N. Bruzy, V. Svitlyk, and G. Garbarino, Comparison between mechanisms and microstructures of α-γ, γ-, and α-α phase transitions in iron, Phys. Rev. B **107**, 104105 (2023).

[40] J. N. Zhou, Y. F. Guo, J. Y. Ren, and X. Z. Tang, The mechanism of hcp-bcc phase transformation in Mg single crystal under high pressure, Scr. Mater. **236**, 115670 (2023).

[41] C. Gao, K. M. Ho, R. M. Wentzcovitch, and Y. Sun, Understanding the two-step nucleation of iron at Earth's inner core conditions: A comparative molecular dynamics study, Phys. Rev. B **111**, 134104 (2025).

[42] B. Sadigh, L. Zepeda-Ruiz, and J. L. Belof, Metastable-solid phase diagrams derived from polymorphic solidification kinetics, Proc. Natl. Acad. Sci. USA **118**, e2017809118 (2021).

[43] S. Azadi, J. S. Wark, and S. M. Vinko, Nonthermal solid-solid phase transition in ferromagnetic iron, Phys. Rev. B **110**, 214434 (2024).

[44] D. Alfè, M. J. Gillan, and G. D. Price, Constraints on the composition of the Earth's core from *ab initio* calculations, Nature (London) **405**, 172 (2000).

[45] Y. Li, L. Vočadlo, D. Alfè, and J. Brodholt, Carbon partitioning between the Earth's inner and outer core, J. Geophys. Res.: Solid Earth **124**, 12812 (2019).

[46] H. Ozawa, K. Hirose, K. Yonemitsu, and Y. Ohishi, High-pressure melting experiments on Fe–Si alloys and implications for silicon as a light element in the core, Earth Planet. Sci. Lett. **456**, 47 (2016).

[47] F. Miozzi, G. Morard, D. Antonangeli, M. Baron, S. Boccato, A. Pakhomova, G. Garbarino, M. Mezouar, and G. Fiquet, Eutectic melting of Fe-3 at Si-4 at C up to 200 GPa and implications for the Earth's core, Earth Planet. Sci. Lett. **544**, 116382 (2020).

[48] S. Tagawa, G. Helffrich, K. Hirose, and Y. Ohishi, High-pressure melting curve of FeH: Implications for eutectic melting between Fe and non-magnetic FeH, J. Geophys. Res.: Solid Earth **127**, e2022JB024365 (2022).

[49] E. Edmund, D. Antonangeli, F. Decremps, F. Miozzi, G. Morard, E. Boulard, A. N. Clark, S. Ayrinhac, M. Gauthier, M. Morand, and M. Mezouar, Velocity-density systematics of Fe-5wt%Si: Constraints on Si content in the Earth's inner core, J. Geophys. Res.: Solid Earth **124**, 3436 (2019).

[50] H. Huang, L. Fan, X. Liu, F. Xu, Y. Wu, G. Yang, C. Leng, Q. Wang, J. Weng, X. Wang, L. Cai, and Y. Fei, Inner core composition paradox revealed by sound velocities of Fe and Fe-Si alloy, Nat. Commun. **13**, 616 (2022).

[51] B. Martorell, I. G. Wood, J. Brodholt, and L. Vočadlo, The elastic properties of hcp-$Fe_{1-x}Si_x$ at Earth's inner-core conditions, Earth Planet. Sci. Lett. **451**, 89 (2016).

[52] Y. He, S. Sun, D. Y. Kim, B. G. Jang, H. Li, and H.-k. Mao, Superionic iron alloys and their seismic velocities in Earth's inner core, Nature (London) **602**, 258 (2022).

[53] https://in.xfel.eu/metadata/doi/10.22003/XFEL.EU-DATA-003063-00.

[54] S. Merkel, G. Morard, E. Edmund, H. Ginestet, Z. Konôpková, M. Anae, D. Antonangeli, K. Appel, O. Ball, M. Baron, S. Boccato, K. Buakor, J. Chantel, H. Cynn, A. Dewaele, A. Dwivedi, L. Ehm, K. Glazyrin, A. Goncharov, H. Graafsma, *et al.*, EuXFEL #3063 experiment on iron and iron alloys under planetary cores conditions [Data set], Zenodo, 2026, https://doi.org/10.5281/zenodo.17950888.